Anisotropy of antiferromagnetic domains in a spin-orbit Mott insulator

Longlong Wu [1,*] Wei Wang,[1] Tadesse A. Assefa,[1,2] Ana F. Suzana,[1] Jiecheng Diao,[3] Hengdi Zhao,[4] Gang Cao,[4] Ross J. Harder,[5] Wonsuk Cha,[5] Kim Kisslinger,[6] Mark P. M. Dean [,1] and Ian K. Robinson [1,3,†]

[1]*Condensed Matter Physics and Materials Science Department, Brookhaven National Laboratory, Upton, New York 11973, USA*
[2]*Stanford Institute for Materials and Energy Sciences, SLAC National Accelerator Laboratory, Menlo Park, California 94025, USA*
[3]*London Centre for Nanotechnology, University College London, London WC1E 6BT, United Kingdom*
[4]*Department of Physics, University of Colorado at Boulder, Boulder, Colorado 80309, USA*
[5]*Advanced Photon Source, Argonne National Laboratory, Illinois 60439, USA*
[6]*Center for Functional Nanomaterials, Brookhaven National Laboratory, Upton, New York 11793, USA*

The temperature-dependent behavior of magnetic domains plays an essential role in the magnetic properties of materials, leading to widespread applications. However, experimental methods to access the three-dimensional (3D) magnetic domain structures are very limited, especially for antiferromagnets. Over the past decades, the spin-orbit Mott insulator iridate Sr_2IrO_4 has attracted particular attention because of its interesting magnetic structure and analogy to superconducting cuprates. Here, we apply resonant x-ray magnetic Bragg coherent diffraction imaging to track the real-space 3D evolution of antiferromagnetic ordering inside a Sr_2IrO_4 single crystal as a function of temperature, finding that the antiferromagnetic domain shows anisotropic changes. The anisotropy of the domain shape reveals the underlying anisotropy of the antiferromagnetic coupling strength within Sr_2IrO_4. These results demonstrate the high potential significance of 3D domain imaging in magnetism research.

In magnetic materials, the formation and dynamics of the magnetic domains play a critical role to determine the macroscopic magnetic properties, such as magnetization and magnetic susceptibility [1–3]. Experimental access to mesoscale structures of magnetic materials can provide information about fundamental magnetic interactions [4–8], which may be related to intrinsic topological properties in the quantum matter [4]. An intriguing Ruddlesden-Popper family of layered two-dimensional (2D) antiferromagnetic spin-orbit Mott insulators, the iridate series $Sr_{n+1}Ir_nO_{3n+1}$, presents an interesting class of frustrated systems, where the spin, orbital, and crystal field interactions conspire to determine the overall electronic configuration [9,10]. Indeed, the single-layer iridate, Sr_2IrO_4, which we study here, already hosts a variety of unconventional magnetism [11]. In Sr_2IrO_4, the narrow electronic band of spin-orbit-split Ir $5d$ states can be further split by the modest on-site Coulomb repulsion to generate an antiferromagnetic Mott insulating state [10,12–14].

The antiferromagnetic Mott ground state of Sr_2IrO_4 can be tuned by different parameters, for example, chemical composition, temperature, strain, and disorder [15,16]. Understanding how magnetic domains respond to the presence of disorder can be detected in their robustness to temperature variations. The structure of Sr_2IrO_4 has been reported to be tetragonal, yet the antiferromagnetic structure breaks this symmetry in the *ab* plane which should lead to orthorhombic domains discussed below. However, x-ray magnetic scattering experiments [17] report the formation of a single magnetic domain orientation in crystals of millimeter size. This is probably due to the presence of some residual strain every time the crystal is cooled in the cryostat. Only in the large samples needed for neutron scattering do the crystals adopt an equal mixture of domain orientations [18]. The antiferromagnetic domain sizes reported in these experiments are all resolution limited, showing that the antiferromagnetic ordering is strong. As a notoriously difficult task, imaging antiferromagnetic structure is accessible to some existing microscopy techniques, for example, x-ray photoemission electron microscopy [19], spin-polarized scanning tunneling microscopy [20], propagation-based phase contrast technique [21], Bragg ptychography [22], and optical second-harmonic generation technique [23,24]. They mainly provide two-dimensional structure information of magnetic materials. Bragg coherent diffractive imaging (BCDI) is a powerful x-ray technique for imaging nanoscale structures in three dimensions [25,26]. It requires a coherent x-ray beam, available from the undulators of third and fourth generation synchrotron sources, such as the Advanced Photon Source (APS). But even there, a large fraction of the available x-ray flux is lost to preserve the beam coherence and so, until now, it has not been possible to overcome the small resonant magnetic cross section to image antiferromagnetic materials.

In this work, we use the resonant x-ray magnetic BCDI approach to study the temperature-dependence evolution of the three-dimensional (3D) image of the antiferromagnetic
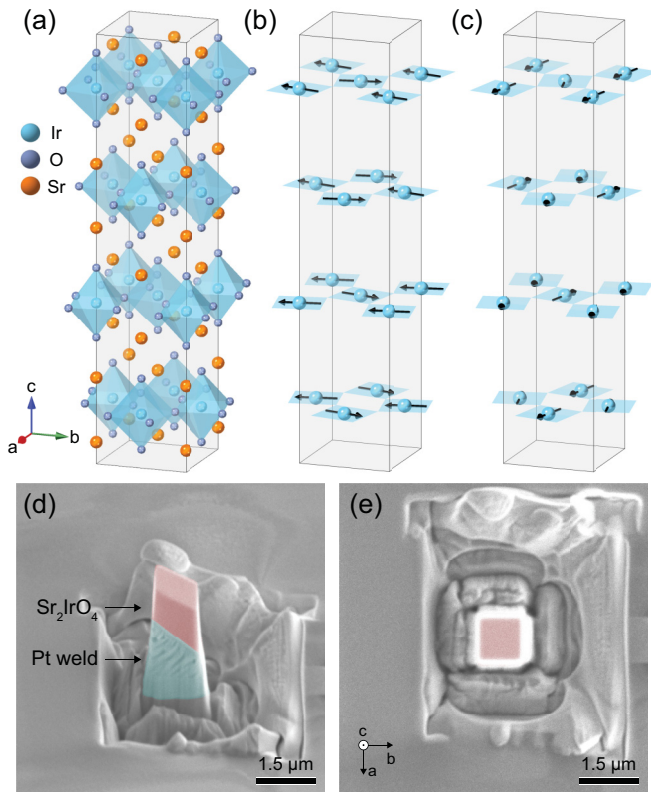
---

*lwu@bnl.gov
†irobinson@bnl.gov

FIG. 1. (a) The crystal structure of Sr_2IrO_4 with space group $I4_1/acd$. (b) *ab* plane canted antiferromagnetic structure. The canting angle of the magnetic moment follows the octahedral rotation rigidly. (c) Corresponding twin domain states of the antiferromagnetic structure. (d) Scanning electron microscopy image of the Sr_2IrO_4 sample from the side view. (e) Top view. The corresponding crystal orientation is indicated in (e).

domains within a Sr_2IrO_4 single crystal. The small Sr_2IrO_4 crystal was fabricated by focused ion beam (FIB) milling. Inverted Bragg coherent diffraction images from the crystal show the formation of antiferromagnetic domains when the temperature of the Sr_2IrO_4 crystal is below the Néel transition temperature $T_N \sim 230$ K. Additionally, from reconstructed images, the estimated antiferromagnetic domain size is ~ 1.1 µm at 120 K and therefore fills the host crystal in the in-plane directions. Upon increasing the temperature, the antiferromagnetic domain is seen to shrink along the *c*-axis direction, suggesting the anisotropic coupling between the Ir spins.

Sr_2IrO_4 has the classic "214" layered perovskite structural motif with the family of cuprate superconductors. Its lattice constants are $a = b = 5.49$ Å and $c = 25.80$ Å at room temperature with tetragonal symmetry (space group $I4_1/acd$), as shown in Fig. 1(a). In Sr_2IrO_4, the square lattice of Ir^{4+} ions are formed by corner-shared IrO_6 octahedra, which elongate and rotate about the *c* axis by $\phi = \sim 11.8°$ [18,27]. Below the Néel temperature $T_N \sim 230$ K, the spin-orbital entangled $J_{eff} = 1/2$ magnetic dipole moments undergo 3D long-range ordering into an orthorhombic antiferromagnetic structure that preserves global inversion symmetry but has lower rotational symmetry. Figures 1(b) and 1(c) show the two canted antiferromagnetic structures on the IrO_2 planes of Sr_2IrO_4, with the black arrows indicating pseudospins and cyan squares

indicating the IrO_2 planes [11,28]. As presented, when the temperature is below T_N, Sr_2IrO_4 has two possible canted antiferromagnetic structures with the net spin moment along the *a* and *b* axes, separately [11,29]. These antiferromagnetic structures are related to the 4_1 screw of the Sr_2IrO_4 lattice structure. As a result, the model of twin antiferromagnetic domain states I and II [i.e., with antiferromagnetic structures described by Figs. 1(b) and 1(c), separately] in Sr_2IrO_4 generate magnetic reflections at $Q_I = (1, 0, 4n + 2)$ and $(0, 1, 4n)$ [28], while for domain state II, the magnetic reflections are presented only at $Q_{II} = (1, 0, 4n)$ and $(0, 1, 4n + 2)$.

The high-quality Sr_2IrO_4 single crystal was grown from off-stoichiometric quantities of $SrCl_2$, $SrCO_3$, and IrO_2 using self-flux techniques [29]. To obtain the microsize crystal needed for the BCDI experiment [30], a large Sr_2IrO_4 crystal was first preoriented crystallographically using a Laue diffractometer, then a block with its size around 1.2 µm was cut out using the FIB lift-out method (see the Supplemental Material [31]). Afterward, the obtained Sr_2IrO_4 crystal was welded with Pt onto a silicon wafer as shown in Figs. 1(d) and 1(e). The selected size of the crystal is less than the penetration depth, ~ 6.6 µm [31] of the 11.218-keV x-ray so that the dynamical diffraction effect is minimized.

The resonant x-ray magnetic BCDI experiment was carried out at the 34-ID-C beamline of the APS, Argonne National Laboratory (see the Supplemental Material [31]). The incident x-ray energy was tuned to the peak of the magnetic signal at 11.218 keV with π polarization, just below the Ir L_3 edge (i.e., the transition from the $2p_{3/2}$ to the $5d$ state) of the Sr_2IrO_4 crystal. During the measurements, the crystal was mounted on a microminiature refrigerator (MMR) stage where the temperature was controlled by an MMR K-20 controller. The MMR technology uses a heat exchanger and Joule-Thompson expansion under a fixed flow of high-pressure nitrogen gas [38,39]. Since the Sr_2IrO_4 crystal was prealigned before the FIB preparation, the crystal alignment was quickly determined using the crystal (204) and (116) peaks with a six-axis diffractometer to maneuver its orientation. The coherent diffraction data were collected by rocking the sample. The crystal (116) and antiferromagnetic (106) peaks were used to study the crystal and magnetic structures, separately.

Figure 2 shows representative Bragg coherent diffraction patterns of the crystal (116) and antiferromagnetic (106) peaks from the Sr_2IrO_4 crystal, converted into reciprocal lattice unit (r.l.u.) coordinates from the detector coordinates. Here, the reciprocal space is indexed with the tetragonal unit cell, defined as $Q = (\frac{2\pi}{a}H, \frac{2\pi}{b}K, \frac{2\pi}{c}L)$. As presented in Figs. 2(a)–2(f), these two Bragg coherent x-ray diffraction patterns have different diffraction fringe distributions but similar directions, indicating their distinct sizes and similar facet orientations in real space between the crystal and antiferromagnetic structures. When the crystal is perfect, for the (116) peak, the coherent x-ray diffraction pattern is mainly determined by the external shape of the crystal. Since the crystal domain size sets an upper limit for the magnetic domain size, the fringe spacings from the antiferromagnetic (106) peak should be similar to or larger than those of the crystal (116) peak.

To explore the effect of temperature on the antiferromagnetic domain in the Sr_2IrO_4 crystal, Fig. 3 shows the integrated x-ray intensity along the [H, 0, 0], [0, K, 0], and
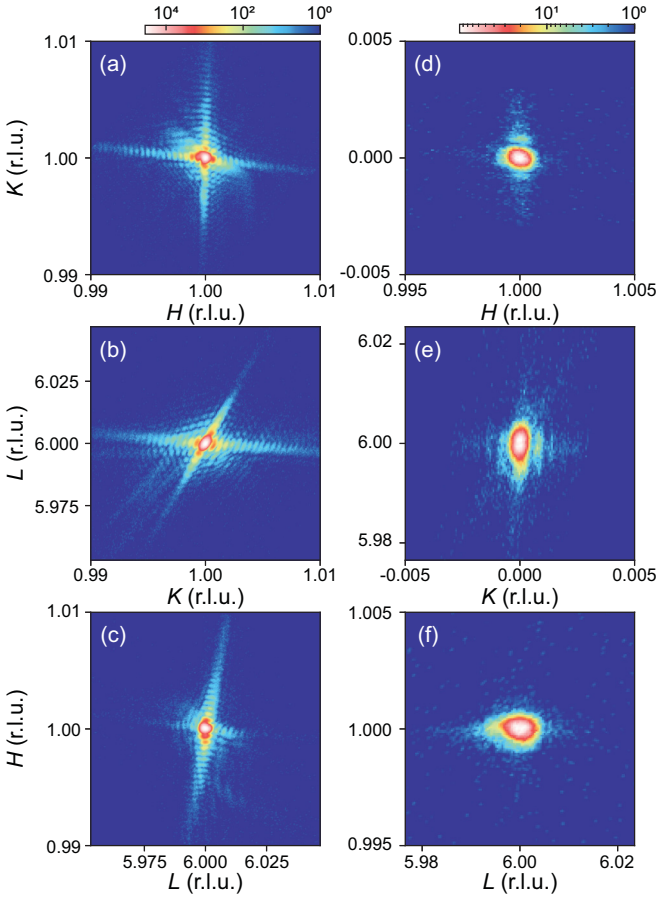
FIG. 2. (a)–(c) Central slice of the 3D reciprocal space mapping around the (116) Bragg peak. (d)–(f) Central slice of the 3D reciprocal space mapping around the antiferromagnetic (106) peak, which was obtained at $T = 120$ K.

[0, 0, L] directions separately from the (106) peak at different selected temperatures and the accompanying (116) peak. Each scan is integrated along the other two transverse r.l.u. directions. As shown in Figs. 3(d)–3(f), the antiferromagnetic peak is getting broader along the [0, 0, L] direction as the temperature is increasing, indicating the antiferromagnetic domain is shrinking along the c-axis direction. However, changes of the peak width in the other two directions are not apparent. To quantitatively determine the effect of the temperature on the antiferromagnetic domain, these one-dimensional line shapes were fitted with pseudo-Voigt functions. Table I

TABLE I. Correlation lengths of the antiferromagnetic domain along different directions at the selected temperature. Here, the second column shows the correlation length of the host crystal itself by using the crystal (116) peak.

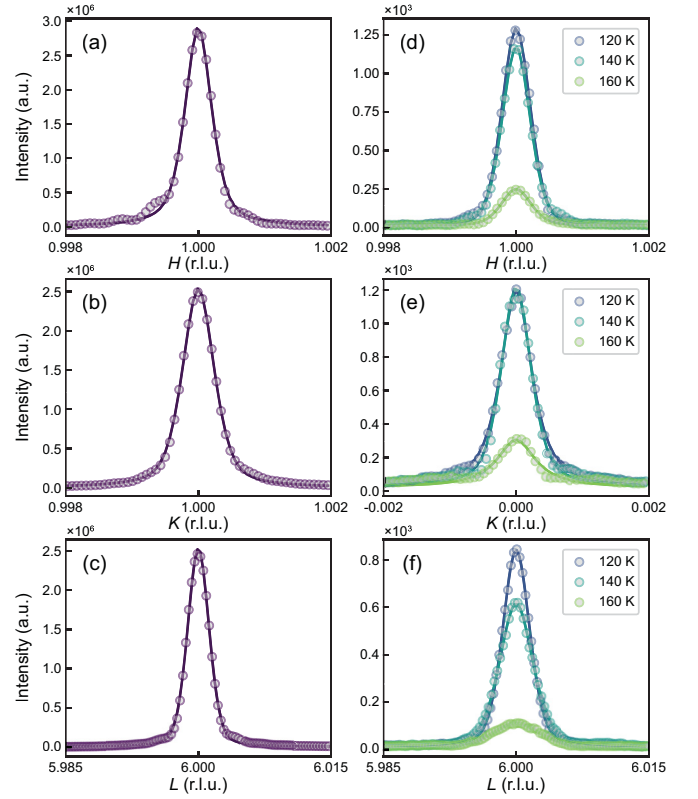| Correlation length (nm)	(116) peak	120 K	140 K	160 K
ξ_H	1153 ± 6	1137 ± 4	1158 ± 4	1030 ± 13
ξ_K	970 ± 3	1019 ± 15	1083 ± 20	871 ± 54
ξ_L	902 ± 3	739 ± 2	610 ± 3	423 ± 9

FIG. 3. (a)–(c) Integrated scan intensity for the wave-vector scan along (a) the [H, 0, 0], (b) the [0, K, 0], and (c) the [0, 0, L] directions from the crystal (116) peak. (d)–(f) Corresponding integrated scan intensity from the antiferromagnetic (106) peak at the selected temperatures along different directions.

shows the corresponding temperature dependence of the correlation length along the different directions, defined as $\xi = d/\mathrm{FWHM}$, where FWHM represents full width at half maximum in reciprocal lattice units and d is the lattice spacing of the appropriate reflection.

We consider that the slightly larger value of the correlation length from the antiferromagnetic (106) peak along the [0, K, 0] direction at 120 and 140 K than that of the crystal (116) peak, seen in Table I, is due to a slight rotation of the Sr_2IrO_4 crystal under illumination with the highly coherent beam, opposite to the scanning direction, as could also be seen from one scan to the next [40]. However, the effect of crystal movement along the other directions, which are mainly parallel to the detector face, is small. Nevertheless, when the temperature is increased to 160 K, the correlation lengths of the antiferromagnetic domain are decreased along all directions by a different amount. This trend indicates a c-axis to a/b-axis anisotropy of the antiferromagnetic coupling strength along different crystal directions. Specifically, the coupling of spins within the IrO_2 a/b plane is indicated to be stronger than between spins between neighboring planes along the c axis.

Compared with the reciprocal-space data fitting method, real-space images can give different details about the temperature-dependent evolution of the antiferromagnetic domain. Since the data in Figs. 2 and 3 were measured with a coherent x-ray beam, the measured coherent x-ray
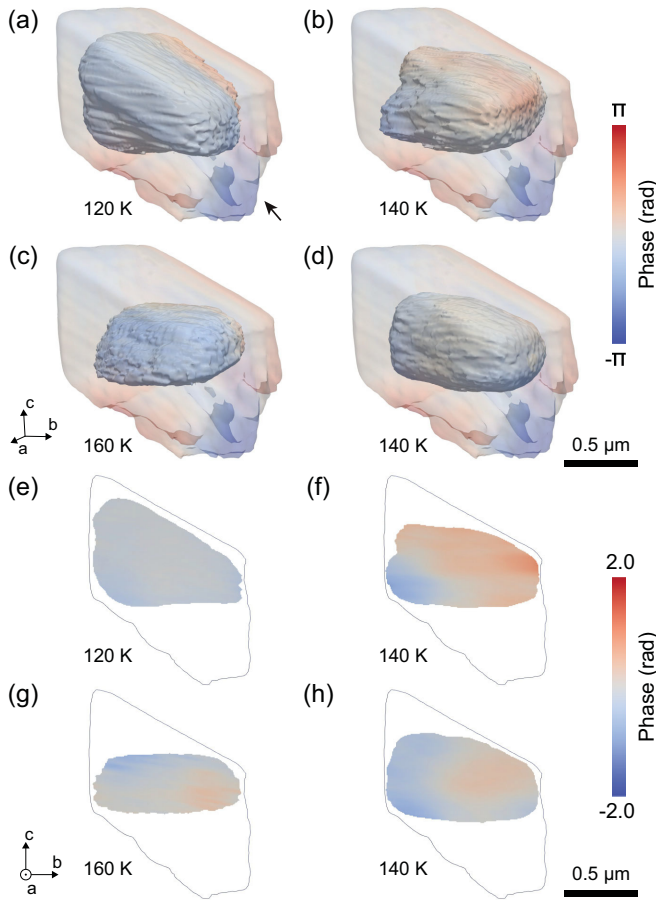
FIG. 4. (a)–(c) Antiferromagnetic domain obtained at $T=$ 120, 140, and 160 K, respectively. (d) Antiferromagnetic domain at $T=$ 140 K after the thermal cycling. Translucent images of the crystal from the (116) peak and isosurface images from the antiferromagnetic (106) peak are superimposed. (e)–(h) Corresponding center slice of (a)–(c). Here, the black lines show the profile of the Sr_2IrO_4 crystal. The antiferromagnetic images were contoured at 25% of the maximum amplitude and colored according to the image phase at the surface.

diffraction patterns can be inverted using the phase retrieval method [35,36]. Figures 4(a)–4(c) show the corresponding reconstructed results using the coherent diffraction data from Figs. 2 and 3. Meanwhile, Figs. 4(e)–4(h) present the corresponding central slice of Figs. 4(a)–4(c). As presented in Fig. 4, the translucent isosurface is obtained from the (116) peak at room temperature, while the inside shows the corresponding antiferromagnetic domain at the different temperatures. Compared with the scanning electron microscope image in Fig. 1, the missing part below the bottom corner of the reconstruction of the Sr_2IrO_4 crystal, as indicated by the black arrow in Fig. 4(a), is probably due to the sample damage induced by the FIB milling process [41,42]. Also, this region of the crystal is found to contain significant strain, indicated by strong phase values in the complex image, interpreted as a projection of the lattice displacement onto the (116) measurement **Q** vector [25]. This and similar behavior confirmed from another Sr_2IrO_4 crystal ($\sim$1.2 μm in size) prepared by the same FIB lift-out method are shown in the Supplemental

Material [31]. As the temperature increases from 120 to 160 K, the antiferromagnetic domain shows an anisotropic change. Especially starting from the top corner of the crystal along the *c*-axis direction, the size of the antiferromagnetic domain decreases much more than in other directions. Additionally, the observed antiferromagnetic domains do not occupy the entire volume of the Sr_2IrO_4 crystal, as shown in Fig. 4(a), most notably in the *c*-axis direction, also seen in Table I. It is possible that these empty regions are filled with the other antiferromagnetic domain orientations, which was not possible to detect using the (016) peak, due to the limited in-plane rotation angle range of the MMR stage. Therefore, we tried to measure the antiferromagnetic (108) peak of this crystal but could not find any magnetic signal, indicating that in these regions the domains with antiferromagnetic spin components along the other direction are too small to be detected or they do not exist. On a larger Sr_2IrO_4 sample ($\sim$8 μm in size), it was checked that when the (106) peak appears, the (108) peak of the other domain also appears (see the Supplemental Material [31]). Thus, as shown in Fig. 4(a), the disappearance of the antiferromagnetic domain in the empty region is possibly related to the strong residual strain induced by the FIB milling process, where the antiferromagnetic domains become orientationally pinned along the *b* axis, which cannot be reached. Another possibility is that the strong strain induced by the FIB milling and Pt-welding process suppresses the formation of the antiferromagnetic domain as a large strain is formed at the bottom corner of the Sr_2IrO_4 crystal. Meanwhile, a weak strain is also observed inside the antiferromagnetic domains, as shown in Fig. 4. While the single antiferromagnetic domain almost fills the crystal in the *a*- and *b*-axis directions, there is a negligible morphological change for the domain near the bottom corner of the crystal when changing the temperature from 120 to 160 K. Away from the bottom corner of the Sr_2IrO_4 crystal, the shortening of the domain size starting from the top corner of the crystal along the *c*-axis direction is most probably due to the relatively weaker out-of-plane spin-spin interaction compared to the in-plane interaction and intrinsic to the iridate compound, but may also be caused by the interaction from the small domains at the top corner, if existing.

It is hard to know the exact locations of the antiferromagnetic domain in the host Sr_2IrO_4 crystal in Fig. 4, since the two images come from independent measurements. In the *a*- and *b*-axis directions, the location is strongly constrained by geometry. But in the *c*-axis direction, there is uncertainty in both the location and how it changes with temperature. The position is likely to be pinned by the strain fields introduced by the FIB milling process. We explored the pinning effect on the antiferromagnetic domain inside the Sr_2IrO_4 sample through thermal cycling experiments. As seen in Fig. 4(d), only one antiferromagnetic domain is formed after thermal cycling, but its shape appears to be slightly rearranged, which suggests that the antiferromagnetic domain is pinned to structural defects in the crystal. However, this could be due to competition between multiple twin domains, resulting in different profiles of the visible antiferromagnetic domain.

Due to the instability of the MMR stage and the limited flux of the third-generation coherent x-ray beam, we consider the

current temperature study to be at its limits, based on many repeated attempts to perform the experiment. In the future, with the development of a high-stability cooling stage and upgrading of the APS storage ring and beamline, we hope to use the resonant BCDI method to investigate the transition of the antiferromagnetic domain in much greater detail to provide insight about the evolution of antiferromagnetic domains near the phase transition. Meanwhile, on a larger length scale, scanning x-ray imaging studies have shown the coexistence of domains with antiferromagnetic spin components along the *a* and *b* axes in the same crystal, separated by hundreds of microns [6]. Since the isolated Sr_2IrO_4 crystal size can be well controlled by the FIB milling process, this method will give us a future opportunity to further utilize multiple crystal and antiferromagnetic peaks to study the effect of the intrinsic strain on the formation of the antiferromagnetic domains. Typically, the damage of sample from FIB is $\sim$20 nm with a 30-keV ion beam and can be further reduced with lower energy beam. Although a 1-keV ion beam was used for the final treatment of our samples to minimize the damage, some of the strains and nonsharp edges could be partly caused by the FIB-milling process.

In conclusion, the resonant x-ray magnetic BCDI method has been applied to study the 3D antiferromagnetic domains inside a small crystal of the spin-orbit Mott insulator Sr_2IrO_4. The results show a distinct anisotropy of the antiferromagnetic domain between the in-plane and *c*-axis directions. Using the obtained real-space images of the antiferromagnetic domain, the detailed morphological evolution of the antiferromagnetic domain inside the crystal has been studied. Upon increasing the temperature, the single antiferromagnetic domain observed shows an anisotropic change in its domain size. A possible reason for this observation is due to the magnetic anisotropy of strontium iridate, arising from its strong spin-orbit coupling and crystal field effect. Our study demonstrates that by using resonance, BCDI can be extended to the purely magnetic diffraction signals arising from antiferromagnetic ordering. With beamline and coherent source improvements, even finer details of magnetic structure could be investigated inside such a crystal. A quantitative analysis of the structure of the antiferromagnetic domains within a single crystal can provide important clues about the lattice spin and charge coupling associated with magnetism. The presented approach will find important applications in systems where complex phases give rise to novel physics. We have demonstrated a way to visualize in three dimensions the antiferromagnetic domains inside an antiferromagnetic material.

[1] P. Nemec, M. Fiebig, T. Kampfrath, and A. V. Kimel, Antiferromagnetic opto-spintronics, Nat. Phys. **14**, 229 (2018).

[2] I. Gross, W. Akhtar, V. Garcia, L. J. Martinez, S. Chouaieb, K. Garcia, C. Carretero, A. Barthelemy, P. Appel, P. Maletinsky, J. V. Kim, J. Y. Chauleau, N. Jaouen, M. Viret, M. Bibes, S. Fusil, and V. Jacques, Real-space imaging of non-collinear antiferromagnetic order with a single-spin magnetometer, Nature (London) **549**, 252 (2017).

[3] A. Scholl, J. Stohr, J. Luning, J. W. Seo, J. Fompeyrine, H. Siegwart, J. Locquet, F. Nolting, S. Anders, E. E. Fullerton, M. R. Scheinfein, and H. A. Padmore, Observation of antiferromagnetic domains in epitaxial thin films, Science **287**, 1014 (2000).

[4] M. G. Kim, A. Barbour, W. Hu, S. B. Wilkins, I. K. Robinson, M. P. M. Dean, J. Yang, C. Won, S. W. Cheong, C. Mazzoli, and V. Kiryukhin, Real-space observation of fluctuating antiferromagnetic domains, Sci. Adv. **8**, eabj9493 (2022).

[5] Y. Hu, T. Zhang, D. Zhao, C. Chen, S. Ding, W. Yang, X. Wang, C. Li, H. Wang, D. Feng, and T. Zhang, Real-space observation of incommensurate spin density wave and coexisting charge density wave on Cr (001) surface, Nat. Commun. **13**, 445 (2022).

[6] T. Choi, Z. Zhang, H. Kim, S. Park, J. W. Kim, K. J. Lee, Z. Islam, U. Welp, S. H. Chang, and B. J. Kim, Nanoscale antiferromagnetic domain imaging using full-field resonant x-ray magnetic diffraction microscopy, Adv. Mater. **34**, e2200639 (2022).

[7] H. Zhao, Z. Porter, X. Chen, S. D. Wilson, Z. Wang, and I. Zeljkovic, Imaging antiferromagnetic domain fluctuations and the effect of atomic scale disorder in a doped spin-orbit Mott insulator, Sci. Adv. **7**, eabi6468 (2021).

[8] J. Li, J. Pelliciari, C. Mazzoli, S. Catalano, F. Simmons, J. T. Sadowski, A. Levitan, M. Gibert, E. Carlson, J. M. Triscone, S. Wilkins, and R. Comin, Scale-invariant magnetic textures in the strongly correlated oxide $NdNiO_3$, Nat. Commun. **10**, 4568 (2019).

[9] S. J. Moon, H. Jin, K. W. Kim, W. S. Choi, Y. S. Lee, J. Yu, G. Cao, A. Sumi, H. Funakubo, C. Bernhard, and T. W. Noh, Dimensionality-controlled Insulator-Metal Transition and Correlated Metallic State in 5d Transition Metal Oxides $Sr_{n+1}Ir_nO_{3n+1}$ (n = 1, 2, and Infinity), Phys. Rev. Lett. **101**, 226402 (2008).

[10] B. J. Kim, H. Jin, S. J. Moon, J. Y. Kim, B. G. Park, C. S. Leem, J. Yu, T. W. Noh, C. Kim, S. J. Oh, J. H. Park, V. Durairaj, G. Cao, and E. Rotenberg, Novel Jeff = 1/2 Mott State Induced

by Relativistic Spin-Orbit Coupling in Sr_2IrO_4, Phys. Rev. Lett. **101**, 076402 (2008).

[11] B. J. Kim, H. Ohsumi, T. Komesu, S. Sakai, T. Morita, H. Takagi, and T. Arima, Phase-sensitive observation of a spin-orbital Mott state in Sr_2IrO_4, Science **323**, 1329 (2009).

[12] M. P. Dean, Y. Cao, X. Liu, S. Wall, D. Zhu, R. Mankowsky, V. Thampy, X. M. Chen, J. G. Vale, D. Casa, J. Kim, A. H. Said, P. Juhas, R. Alonso-Mori, J. M. Glownia, A. Robert, J. Robinson, M. Sikorski, S. Song, M. Kozina *et al.*, Ultrafast energy- and momentum-resolved dynamics of magnetic correlations in the photo-doped Mott insulator Sr_2IrO_4, Nat. Mater. **15**, 601 (2016).

[13] J. Bertinshaw, Y. K. Kim, G. Khaliullin, and B. J. Kim, Square lattice iridates, Annu. Rev. Condens. Matter Phys. **10**, 315 (2019).

[14] C. Martins, M. Aichhorn, L. Vaugier, and S. Biermann, Reduced Effective Spin-Orbital Degeneracy and Spin-Orbital Ordering in Paramagnetic Transition-Metal Oxides: Sr_2IrO_4 Versus Sr_2RhO_4, Phys. Rev. Lett. **107**, 266404 (2011).

[15] E. Paris, Y. Tseng, E. M. Parschke, W. Zhang, M. H. Upton, A. Efimenko, K. Rolfs, D. E. McNally, L. Maurel, M. Naamneh, M. Caputo, V. N. Strocov, Z. Wang, D. Casa, C. W. Schneider, E. Pomjakushina, K. Wohlfeld, M. Radovic, and T. Schmitt, Strain engineering of the charge and spin-orbital interactions in Sr_2IrO_4, Proc. Natl. Acad. Sci. USA **117**, 24764 (2020).

[16] F. Ye, S. Chi, B. C. Chakoumakos, J. A. Fernandez-Baca, T. Qi, and G. Cao, Magnetic and crystal structures of Sr_2IrO_4 : A neutron diffraction study, Phys. Rev. B **87**, 140406(R) (2013).

[17] S. Boseggia, H. C. Walker, J. Vale, R. Springell, Z. Feng, R. S. Perry, M. Moretti Sala, H. M. Ronnow, S. P. Collins, and D. F. McMorrow, Locking of iridium magnetic moments to the correlated rotation of oxygen octahedra in Sr_2IrO_4 revealed by x-ray resonant scattering, J. Condens. Matter Phys. **25**, 422202 (2013).

[18] M. K. Crawford, M. A. Subramanian, R. L. Harlow, J. A. Fernandez-Baca, Z. R. Wang, and D. C. Johnston, Structural and magnetic studies of Sr_2IrO_4, Phys. Rev. B **49**, 9198 (1994).

[19] S. Anders, H. A. Padmore, R. M. Duarte, T. Renner, T. Stammler, A. Scholl, M. R. Scheinfein, J. Stohr, L. Seve, and B. Sinkovic, Photoemission electron microscope for the study of magnetic materials, Rev. Sci. Instrum. **70**, 3973 (1999).

[20] M. Bode, E. Y. Vedmedenko, K. von Bergmann, A. Kubetzka, P. Ferriani, S. Heinze, and R. Wiesendanger, Atomic spin structure of antiferromagnetic domain walls, Nat. Mater. **5**, 477 (2006).

[21] M. G. Kim, H. Miao, B. Gao, S. W. Cheong, C. Mazzoli, A. Barbour, W. Hu, S. B. Wilkins, I. K. Robinson, M. P. M. Dean, and V. Kiryukhin, Imaging antiferromagnetic antiphase domain boundaries using magnetic Bragg diffraction phase contrast, Nat. Commun. **9**, 5013 (2018).

[22] L. Wu, Y. Shen, A. M. Barbour, W. Wang, D. Prabhakaran, A. T. Boothroyd, C. Mazzoli, J. M. Tranquada, M. P. M. Dean, and I. K. Robinson, Real Space Imaging of Spin Stripe Domain Fluctuations in a Complex Oxide, Phys. Rev. Lett. **127**, 275301 (2021).

[23] L. Zhao, D. H. Torchinsky, H. Chu, V. Ivanov, R. Lifshitz, R. Flint, T. Qi, G. Cao, and D. Hsieh, Evidence of an odd-parity hidden order in a spin–orbit coupled correlated iridate, Nat. Phys. **12**, 32 (2015).

[24] K. L. Seyler, A. de la Torre, Z. Porter, E. Zoghlin, R. Polski, M. Nguyen, S. Nadj-Perge, S. D. Wilson, and D. Hsieh, Spin-orbit-enhanced magnetic surface second-harmonic generation in Sr_2IrO_4, Phys. Rev. B **102**, 201113(R) (2020).

[25] I. Robinson and R. Harder, Coherent X-ray diffraction imaging of strain at the nanoscale, Nat. Mater. **8**, 291 (2009).

[26] J. Miao, T. Ishikawa, I. K. Robinson, and M. M. Murnane, Beyond crystallography: Diffractive imaging using coherent x-ray light sources, Science **348**, 530 (2015).

[27] Q. Huang, J. L. Soubeyroux, O. Chmaissem, I. Natalisora, A. Santoro, R. J. Cava, J. J. Krajewski, and W. F. Peck, Neutron powder diffraction study of the crystal-structures of Sr_2RuO_4 and Sr_2IrO_4 at room-temperature and at 10-K, J. Solid State Chem. **112**, 355 (1994).

[28] C. Dhital, T. Hogan, Z. Yamani, C. de la Cruz, X. Chen, S. Khadka, Z. S. Ren, and S. D. Wilson, Neutron scattering study of correlated phase behavior in Sr_2IrO_4, Phys. Rev. B **87**, 144405 (2013).

[29] G. Cao, J. Bolivar, S. McCall, J. E. Crow, and R. P. Guertin, Weak ferromagnetism, metal-to-nonmetal transition, and negative differential resistivity in single-crystal Sr_2IrO_4, Phys. Rev. B **57**, R11039(R) (1998).

[30] T. A. Assefa, Y. Cao, J. Diao, R. J. Harder, W. Cha, K. Kisslinger, G. D. Gu, J. M. Tranquada, M. P. M. Dean, and I. K. Robinson, Scaling behavior of low-temperature orthorhombic domains in the prototypical high-temperature superconductor $La_{1.875}Ba_{0.125}CuO_4$, Phys. Rev. B **101**, 054104 (2020).

[31] See Supplemental Material at http://link.aps.org/supplemental/10.1103/PhysRevB.108.L020403 for details about sample preparation, x-ray measurements and setup, BCDI reconstruction, strain calculation, penetration depth estimation, comparison of reconstructed Sr_2IrO_4 structures with different sizes, and antiferromagnetic Bragg reflections from the $\sim$ 8-um sample. The Supplemental Material also contains Refs. [32–37].

[32] M. P. Dean, G. Dellea, R. S. Springell, F. Yakhou-Harris, K. Kummer, N. B. Brookes, X. Liu, Y. J. Sun, J. Strle, T. Schmitt, L. Braicovich, G. Ghiringhelli, I. Bozovic, and J. P. Hill, Persistence of magnetic excitations in $La_{2-x}Sr_xCuO_4$ from the undoped insulator to the heavily overdoped non-superconducting metal, Nat. Mater. **12**, 1019 (2013).

[33] D. Paganin, *Coherent X-ray Optics* (Oxford University Press, Oxford, 2006).

[34] D. Haskel, G. Fabbris, M. Zhernenkov, P. P. Kong, C. Q. Jin, G. Cao, and M. van Veenendaal, Pressure Tuning of the Spin-Orbit Coupled Ground State in Sr_2IrO_4, Phys. Rev. Lett. **109**, 027204 (2012).

[35] L. Wu, S. Yoo, A. F. Suzana, T. A. Assefa, J. C. Diao, R. J. Harder, W. Cha, and I. K. Robinson, Three-dimensional coherent X-ray diffraction imaging via deep convolutional neural networks, Npj Comput. Mater. **7**, 175 (2021).

[36] L. Wu, P. Juhas, S. Yoo, and I. Robinson, Complex imaging of phase domains by deep neural networks, IUCrJ **8**, 12 (2021).

[37] S. Marchesini, H. He, H. N. Chapman, S. P. Hau-Riege, A. Noy, M. R. Howells, U. Weierstall, and J. C. H. Spence, X-ray image reconstruction from a diffraction pattern alone, Phys. Rev. B **68**, 140101(R) (2003).

[38] W. Peiyi and W. A. Little, Measurement of friction factors for the flow of gases in very fine channels used for microminiature Joule-Thomson refrigerators, Cryogenics **23**, 273 (1983).

[39] H. Geng, X. Y. Cui, J. H. Weng, H. L. She, and W. Q. Wang, Review of experimental research on Joule-Thomson cryogenic refrigeration system, Appl. Therm. Eng. **157**, 113640 (2019).

[40] M. Monteforte, A. K. Estandarte, B. Chen, R. Harder, M. H. Huang, and I. K. Robinson, Novel silica stabilization method for the analysis of fine nanocrystals using coherent X-ray diffraction imaging, J. Synchrotron Radiat. **23**, 953 (2016).

[41] F. Hofmann, E. Tarleton, R. J. Harder, N. W. Phillips, P. W. Ma, J. N. Clark, I. K. Robinson, B. Abbey, W. Liu, and C. E. Beck, 3D lattice distortions and defect structures in ion-implanted nano-crystals, Sci. Rep. **7**, 45993 (2017).

[42] N. I. Kato, Reducing focused ion beam damage to transmission electron microscopy samples, J. Electron Microsc. (Tokyo) **53**, 451 (2004).